Rate- and strain-dependent brittle deformation of rocks

N. Brantut[1], M. J. Heap[2], P. Baud[2], and P. G. Meredith[1]

[1]Rock and Ice Physics Laboratory, Department of Earth Sciences, University College London, London, UK, [2]Laboratoire de Déformation des Roches, Géophysique Expérimentale, Institut de Physique de Globe de Strasbourg (UMR 7516 CNRS, Université de Strasbourg/EOST), Strasbourg, France

Abstract We develop a unifying framework to quantify rate-dependent deformation in the brittle field and establish links between the microscale time-dependent crack growth processes and the macroscopically observed rate dependency. Triaxial deformation experiments have been performed under both constant strain rate and constant stress (creep) conditions on three types of sandstone. The measured relative evolution of P wave speeds as a function of inelastic axial strain is similar for both types of test, despite differences in strain rate of up to 3 orders of magnitude. This similarity indicates that there exists a direct, time-independent link between the microstructural state (as reflected by the variations in P wave speed) and the inelastic axial strain. Comparison of applied stresses between constant strain rate and creep experiments as a function of inelastic strain indicates that creep deformation requires less mechanical work to bring the sample to failure. This energy deficit corresponds to a stress deficit, which can be related to a deficit in energy release rate of the microcracks. We establish empirically that the creep strain rate is given by $\dot{\epsilon} \propto \exp(\Delta Q/\sigma^*)$, where ΔQ is the stress deficit (negative) and σ^* is an activation stress. This empirical exponential relation between creep strain rate and stress deficit is analogous to rate-and-state friction law. We develop a micromechanical approach based on fracture mechanics to determine the evolution of an effective stress intensity factor at crack tips during creep deformation and estimate the activation volume of the stress corrosion reaction responsible for brittle creep.

1. Introduction

Fracturing is the most prevalent deformation mechanism in rocks under upper crustal conditions. Cracks in rocks occur from the grain scale up to the crustal scale. Under all round compressive stress conditions, macroscopic fractures or faults (at the scale of centimeters and above) result from the coalescence of many microscopic, grain-scale cracks [*Paterson and Wong*, 2005]. Slip along preexisting fault zones and discontinuities generally also requires fracturing at local contacts or asperities. Reactivation of ancient, healed fault zones involves refracturing of cemented, cohesive rock masses. Hence, brittle deformation of intact (i.e., cohesive) rocks is expected to be one of the fundamental underlying processes of fault formation, growth, and sliding.

Deformation in the crust occurs over a wide range of strain rates, from the very slow rates associated with tectonic loading (of the order of 10^{-14} s^{-1} or lower) up to the very fast rates occurring during earthquakes (of the order of 10^3 s^{-1} or higher). Hence, a complete understanding of fault mechanics requires a detailed knowledge of the time-dependent mechanical behavior of rocks. Such a knowledge should be based on micromechanics but also provide an adequate macroscopic description. The goal of this paper therefore is to establish a simple macroscopic description of the rate dependency of brittle deformation and to link it quantitatively to the corresponding microscale processes. To achieve this, a key challenge is the determination of a relationship between the internal or microstructural state of the rock and macroscopically observable quantities.

As stated above, deformation of rocks in the brittle field proceeds by the progressive growth and coalescence of microcracks. Under nominally dry environmental conditions and rapid loading, crack growth is primarily governed by the applied stresses. Indeed, laboratory experiments show that rock strength is essentially time independent under such conditions [*Paterson and Wong*, 2005]. At the microscopic scale, time independence means that the crack growth criterion is well modeled by the concept of constant fracture toughness, i.e., a critical stress intensity factor at microcrack tips. At lower strain rates and in the presence of aqueous fluids, i.e., under realistic upper crustal conditions, experiments show that rock fracturing
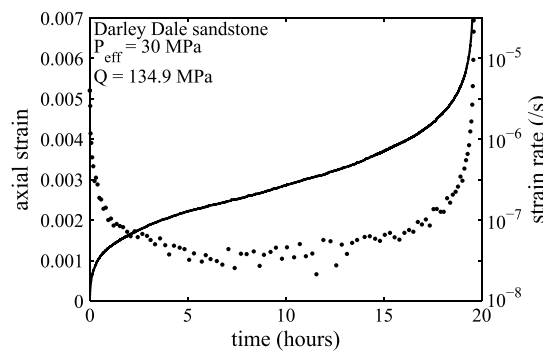
Figure 1. Typical strain and strain rate versus time behavior during brittle creep. Experiment performed on a cylindrical sample of Darley Dale sandstone, in a triaxial stress state at an effective pressure of $P_{eff} = 30$ MPa and a constant differential stress $Q = 134.9$ MPa.

becomes time dependent. This is well demonstrated by the fact that rocks can fail by static fatigue, following a preceding period of creep deformation, under conditions of constant applied stress [e.g., *Scholz*, 1968; *Kranz*, 1979, 1980; *Kranz et al.*, 1982; *Baud and Meredith*, 1997; *Heap et al.*, 2009; *Brantut et al.*, 2013b]. Time-dependent crack growth arises from chemically activated subcritical crack growth processes, such as stress corrosion reactions [see *Atkinson*, 1984]. Establishing quantitative links between microscopic, grain-scale subcritical cracking and macroscopic, sample-scale to crustal scale brittle creep behavior is a key challenge for our understanding of the time-dependent mechanics of rocks in the Earth's crust.

Experimental rock deformation provides us with several ways to investigate time-dependent brittle deformation. Two main types of experiments can be distinguished: (1) "constant strain rate" experiments in which stress varies as a result of deformation and (2) "creep" experiments in which deformation and deformation rate vary over time as a result of an imposed constant stress.

In the latter case, when a rock is held at constant stress (i.e., both the differential stress, denoted Q, and the effective confining pressure, denoted P_{eff}, are maintained constant), it deforms typically in the manner depicted in Figure 1. Three deformation stages have commonly been described, based solely on the observed macroscopic strain-time behavior: an initial decelerating stage, termed primary creep, followed by an apparent constant strain rate stage, termed secondary creep, and finally an accelerating tertiary creep stage, after which the sample fails. It is apparent from Figure 1 that the rock experiences a wide range of strain rates as deformation proceeds. Such experiments hence convey very rich information on the time dependency of the brittle deformation process. However, results from brittle creep experiments are usually used to extract only times to failure and/or secondary creep strain rates, as functions of the applied differential stress, effective pressure, and/or temperature (see *Brantut et al.* [2013b] for a review). The extraction of a single strain rate from a complete nonlinear strain-time curve evidently obscures the richness and complexity inherent in the creep process. A more comprehensive approach to understand the creep process as a whole, including the primary and tertiary creep stages, remains to be developed.

More generally, if a consistent description of time-dependent brittle deformation is to be determined, it should explain *in a unified manner* both creep (constant stress) and constant strain rate deformation. In a recent theoretical study [*Brantut et al.*, 2012], we used a micromechanical framework to show how the increasing importance of microcrack interactions with increasing microcrack size could produce the switch from decreasing to increasing crack growth rate during deformation at constant stress (i.e., the transition from primary to tertiary creep). It is the same process that is in fact responsible for the existence of a peak stress in deformation experiments performed at imposed strain rate [*Ashby and Sammis*, 1990]. The specific theoretical approach of *Brantut et al.* [2012] hence provides a consistent understanding of the rock fracturing process as a whole and in particular establishes a link between the evolution of strain rate during tests at imposed stress and the evolution of stress during tests at imposed strain rates. However, the model of *Brantut et al.* [2012] is based on strong assumptions about the microcrack geometry, which are appropriate for modeling low porosity crystalline rocks but are not necessarily appropriate for other rock microstructures.

In this paper, we aim to establish a unified understanding of time-dependent mechanical behavior of rock in the brittle regime, specifically focusing on creep deformation. Our approach is based on the analysis of a new set of data obtained on a range of sandstones under triaxial loading conditions. Section 2 summarizes the sample materials and experimental techniques used in our study. Then, in section 3, we present new experimental results from elastic wave velocity measurements made during both creep and constant strain rate deformation. Because elastic wave velocities are very sensitive to microcrack density and orientation,

these results allow us to determine how microcracks develop as a function of the inelastic deformation of the samples and hence provide us with an empirical relation between the *internal state* of the samples and macroscopically observable quantities such as the inelastic axial strain. In section 4, we analyze the results of the triaxial deformation experiments by comparing, for each increment of change in internal state, the stress and energy required to deform the rock samples under both creep and constant strain rate conditions. This analysis provides us with an empirical relation between stress and strain rate which is *valid for the whole creep process* (and not just during "secondary" creep). Section 5 is dedicated to the determination of the link between the observed, macroscopic creep law and the underlying microscale subcritical cracking process. To achieve this, we develop a novel, general methodology that allows the determination of empirical micromechanical functions linking the local effective stress intensity factor at microcrack tips to the applied stresses. Finally, we discuss the impact and significance of our results in section 6.

2. Experimental Methods

2.1. Starting Materials and Sample Preparation

Porous sandstones from Darley Dale (northern England) and Bentheim and Wertheim (Germany) were used. Darley Dale and Wertheim sandstones are quartzo-feldspathic; Darley Dale sandstone contains 66% quartz and 21% feldspar, and Wertheim sandstone contains 58% quartz and 33% feldspar. Their average porosity is similar at around 13% [*Klein and Reuschlé*, 2004; *Heap et al.*, 2009]. Bentheim sandstone is composed mostly of quartz (95%), and its average porosity is 23% [*Baud et al.*, 2006]. Porosities of individual samples are reported in Table 1. Cylindrical samples were prepared by coring sandstone blocks and grinding the ends of the cores to ensure parallelism of the two end surfaces (to ± 10 μm accuracy). All the samples were saturated with distilled water for at least 24 h before testing. All saturated samples were then jacketed in an impermeable rubber sleeve before insertion into the deformation apparatus.

2.2. Triaxial Deformation Experiments

Deformation tests were performed in conventional triaxial apparatus at the Experimental Geophysics Laboratory of the University of Strasbourg (see full description in *Baud et al.* [2009]) and at the Rock and Ice Physics Laboratory of University College London (UCL) (see description in *Eccles et al.* [2005]). Both machines are capable of applying servo-controlled axial load, confining pressure, and pore fluid pressure. The axial shortening of the samples were measured with linear voltage differential transducers (LVDTs) positioned outside the pressure vessel, and the shortening was corrected for the deformation of the loading train. All tests were performed under drained, constant pore pressure conditions. Pore volume changes were monitored by measuring (with an LVDT) the displacement of the actuators applying the servo-controlled pore fluid pressure. We use the change in pore volume to estimate the bulk volumetric strain, assuming constant solid volume. A summary of the samples tested and experimental conditions is presented in Table 1. All experiments were performed in the brittle regime, i.e., all samples failed by localized shear faulting.

Two types of experiment were performed. Samples were deformed either under constant strain rate ($\dot{\varepsilon} = 10^{-5}$ s^{-1}) or under constant differential stress (creep) conditions. In the latter case, the samples were initially loaded at constant strain rate (10^{-5} s^{-1}) until the target differential stress was reached. Then, the differential stress was held constant (using a servo-control system) throughout the remainder of the experiment as the sample deformed over time (see *Brantut et al.* [2013b] for more details).

2.3. Wave Velocity Measurements

For some targeted deformation tests on Darley Dale sandstone (both creep and constant strain rate), the evolution of elastic wave velocities with increasing deformation was measured. Here we describe the technique used.

The UCL triaxial apparatus is equipped with 10 piezoelectric transducers positioned around the sample as shown in Figure 2, connected to a 10 MHz digital recording system. Repeatedly during the tests, a high-voltage ($\sim$100 V), high-frequency ($\sim$1 MHz) pulse was sent sequentially to each transducer, hence producing a mechanical wave with known origin time, while output waveforms were recorded on the nine remaining transducers. Precise *P* wave arrival times were extracted from the waveform data by using the cross-correlation technique described by *Brantut et al.* [2011]; the method was improved by resampling the cross-correlation results with interpolated cubic splines, and the resulting precision on the arrival times was 0.05 μs (i.e., around 0.5% relative error on the wave speed). The arrival times were then used to determine the relative *P* wave speed evolution throughout the tests.

Table 1. Summary of the Samples Tested and Experimental Conditions[a]

Rock Type	Sample	Porosity (%)	P_{eff} (MPa)	Strain Rate (s^{-1})	Peak Differential Stress (MPa)	Creep Differential Stress (MPa)	Time to Failure (s)	Notes
Darley Dale	dd3	13.8	10	10^{-5}	88.9	–	–	
Darley Dale	dd9	14.1	10	–	–	79.3	$1.9\,10^5$	
Darley Dale	dd4	14.1	10	–	–	82.7	$5.6\,10^3$	
Darley Dale	dd2	13.8	10	–	–	83.3	$6.2\,10^4$	
Darley Dale	dd5	14.3	10	–	–	85.9	$1.4\,10^4$	
Darley Dale	dds2w	14.4	20	10^{-5}	121.8	–	–	
Darley Dale	dds11w	14.3	20	–	–	108.4	$4.5\,10^5$	
Darley Dale	dds7w	14.4	20	–	–	112.0	$5.3\,10^4$	
Darley Dale	dds6w	14.3	20	–	–	113.7	$7.0\,10^3$	
Darley Dale	dds1w	14.1	30	10^{-5}	147.2	–	–	
Darley Dale	dds13w	14.2	30	–	–	134.9	$7.1\,10^4$	
Darley Dale	dds8w	14.1	30	–	–	138.8	$7.1\,10^3$	
Darley Dale	dds14w	13.3	40	10^{-5}	168.4	–	–	
Darley Dale	dds9w	13.2	40	–	–	161.8	$6.7\,10^3$	
Darley Dale	dds12w	13.2	40	–	–	162.4	$1.2\,10^4$	
Darley Dale	dds-c2-09	12.9	40	10^{-5}	163.6	–	–	V_P monitored
Darley Dale	dds-c2-34	12.7	40	–	–	154.7	$3.5\,10^4$	V_P monitored
Darley Dale	dds-c2-13	13.4	40	–	–	157.0	$6.1\,10^3$	V_P monitored
Bentheim	ben4	22.6	10	10^{-5}	116.1	–	–	
Bentheim	ben10t	22.7	10	10^{-5}	119.0	–	–	
Bentheim	ben20t	22.2	20	10^{-5}	160.3	–	–	
Bentheim	ben30t	22.2	30	10^{-5}	177.9	–	–	
Bentheim	ben12	22.6	10	–	–	108.8	$1.5\,10^5$	
Bentheim	ben7	22.4	10	–	–	112.9	$9.7\,10^3$	
Wertheim	we6	12.6	10	10^{-5}	115.5	–	–	
Wertheim	we4	13.1	10	–	–	95.1	$7.8\,10^5$	
Wertheim	we11	12.7	10	–	–	100.7	$8.7\,10^3$	
Wertheim	we3	12.4	10	–	–	102.3	$2.5\,10^4$	
Wertheim	we2	13.0	10	–	–	106.3	$4.9\,10^3$	

[a]For experiments performed under constant strain rate conditions, we report both the imposed strain rate and the observed peak differential stress. For experiments performed under creep conditions, we report the imposed differential stress and time to failure.

The array of transducers, the positions of which are reported in Figure 2, allowed the determination of P wave speeds along four different orientations with respect to the axis of compression: 90° (radial), 39°, 58°, and 28°. For each set of measurements, the relative P wave speeds were fitted to a transversely isotropic elastic model, assuming weak anisotropy [*Thomsen*, 1986]:

$$V(\theta) = \frac{1}{2}(V_{axial} + V_{radial}) - \frac{1}{2}(V_{axial} - V_{radial})\cos(\pi - 2\theta), \tag{1}$$

where θ is the angle between the compression axis and the ray path, V_{axial} is the P wave speed along the compression axis, and V_{radial} is the P wave speed perpendicular to the compression axis. V_{axial} was estimated from a least squares inversion of the measured velocities along the four available propagation angles. Relation (1) allowed us to fully describe the wave velocities with only two independent parameters, V_{axial} and V_{radial}.

2.4. Inelastic Strain Calculations
For each test, the sample's initial Young's modulus was determined from a fit of the linear part of the differential stress versus axial strain curves. This allowed the nominal elastic strain at any stress to be determined (i.e., the strain that the intact material would have had at the same level of stress) and subtracted from the total recorded axial strain to obtain the inelastic axial strain. In this process, the initial, nonlinear deformation (typically of the order of 0.02%), which correspond to both sample assembly adjustments and closure of preexisting subhorizontal microcracks within the sample [see *David et al.*, 2012], was also subtracted from the total inelastic axial strain.

2.5. Strain Rate Calculations
The recording interval of stress, strain, and pore volume was deliberately varied (within the range 1 s to 1 min) in line with the very wide range in test durations. Also, the calculation of a time derivative such as strain rate from a discretely recorded signal is nontrivial because high frequency noise is amplified when taking differences between successive time steps. We therefore developed a specific method based on
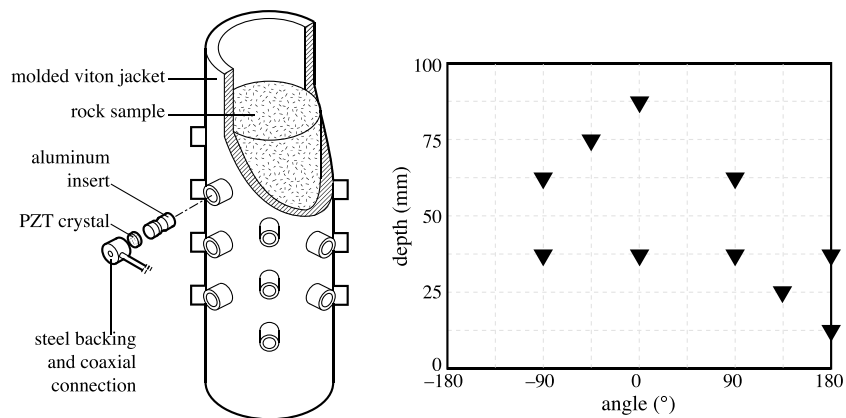
Figure 2. (left) Isometric view of the sample and sample jacket used in the UCL system. Sample diameter is 40 mm, and length is 100 mm. Ten acoustic transducers were mounted on molded inserts in the jacket. Unused inserts were blanked with aluminum plugs. (right) Map of sensor positions around the sample.

Chebyshev interpolation to circumvent this problem. The instantaneous strain rate was estimated as follows. The creep time was mapped to the interval $[-1, 1]$, and the strain-time curve was interpolated on N Chebyshev-Lobatto nodes ($40 \leq N \leq 100$, depending on the total number of initial data points). The derivative of strain with respect to the normalized time was then obtained by multiplying the $N \times N$ Chebyshev differentiation matrix by the vector formed with the N interpolated points (details of the method and computation can be found in *Trefethen* [2000]). The strain rate was finally obtained by mapping back the time from the normalized $[-1, 1]$ interval to the real creep time in seconds (i.e., from 0 to the time to failure) and reinterpolated on all the recorded time steps. This last stage does not improve the quality of the strain rate estimates but is useful to enable all the variables (stress, strain, etc.) to be correlated within a single time scale.

3. Inelastic Strain as a Proxy for Internal State

In this study we want to compare stresses and strain rates between creep (constant applied stress) and constant applied strain rate tests. Such a comparison is meaningful only if it is performed for samples at the same microstructural state. We thus need to determine a physical quantity that reflects the overall microstructural state of the samples and that we can measure systematically throughout our experiments. In the brittle regime, evolution of the microstructural state during deformation corresponds primarily to the growth of dilatant microcracks between or inside the grains [e.g., *Scholz*, 2002; *Paterson and Wong*, 2005]. Because they are traction-free internal surfaces, such microcracks have a strong influence on the elastic wave speeds of rocks [e.g., *Sayers and Kachanov*, 1995; *Fortin et al.*, 2007]. Hence, by monitoring the evolution of elastic wave speeds during deformation under both creep and constant strain rate conditions, we have an indirect measure of the microstructural state of the samples (i.e., microcrack density and orientation). Here we present the wave speed measurements performed during selected experiments and use them to determine how inelastic axial strain can be used as a convenient proxy for microstructural state.

Figure 3 shows the evolution of the measured P wave speeds, in four different orientations with respect to the axis of compression, as a function of total axial strain, for one constant strain rate experiment (Figure 3a) and two creep experiments (Figures 3b and 3c) performed on Darley Dale sandstone at $P_{eff} = 40$ MPa (samples dd-c2-09, dd-c2-13, and dd-c2-34 in Table 1). The initial P wave speed at $P_{eff} = 40$ MPa before deformation is around 4.3 ± 0.1 km s^{-1}. The evolution of P wave speed with increasing axial deformation follows a well-known pattern [e.g., *Ayling et al.*, 1995], which appears to be common to both types of test. The radial P wave speed (circle symbols) monotonically decreases with increasing axial deformation. Concomitantly, the P wave speeds measured along lower angles to the compression axis, namely, 58° (squares), 39° (diamonds), and 28° (triangles), initially increase at the onset of axial deformation and subsequently decrease after around 0.6% axial strain. The total decrease in P wave speed is larger along the radial direction than along the subaxial directions. This evolution is typical of rocks that crack progressively under compression [*Paterson and Wong*, 2005, chap. 5]: when the differential stress is applied, the rock initially behaves elastically, with subradial cracks closing (hence the initial increase in subaxial P wave speeds), while
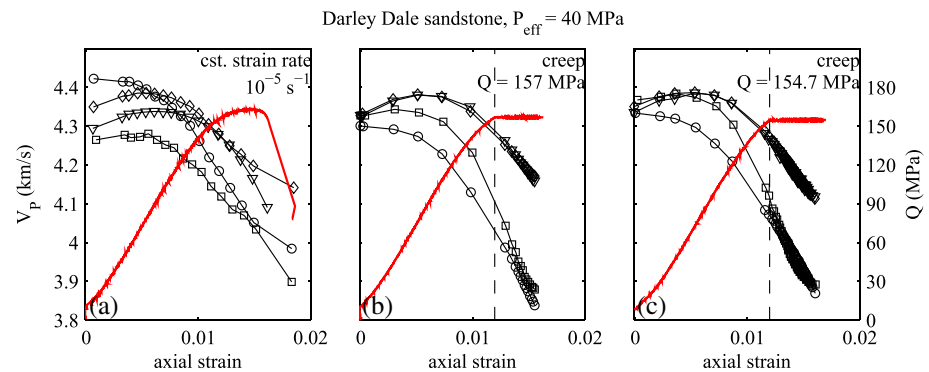
Figure 3. Differential stress (red) and evolution of *P* wave speeds as a function of total axial strain during triaxial deformation tests performed on Darley Dale sandstone at P_{eff} = 40 MPa, under (a) constant strain rate and (b and c) creep. Dotted lines in Figures 3b and 3c mark the start of creep. Symbols correspond to the various orientations with respect to the axis of compression: 90° (radial; circles), 58° (squares), 39° (diamonds), and 28° (inverted triangles). Sample reference numbers are, from left to right: dd-c2-09, dd-c2-13, and dd-c2-34, respectively (see Table 1).

subaxial cracks begin to open. Then, when the stress threshold for crack propagation is reached, i.e., after some amount of axial strain, cracks open preferentially in the subaxial direction (hence the large decrease in the radial *P* wave speed). We hence observe the development of a crack-induced anisotropy.

Comparison of Figures 3a, 3b, and 3c reveals not only that the qualitative evolution of the *P* wave speeds is similar for both creep and constant strain rate deformation conditions but also that the quantitative changes in *P* wave speeds (aside from some variability in the initial values) are remarkably similar. Despite several orders of magnitude difference in times to failure (and therefore in strain rate), the rate of decrease in *P* wave speed per unit of axial strain appears to be similar for all three tests. This observation suggests that axial strain is a potential proxy for the microstructural state of the samples. However, a significant part of the total axial strain corresponds to the elastic deformation of the specimen, and hence differences in applied differential stress from one experiment to another will generate differences in axial strain that are not due solely to crack growth. This introduces a bias that can be avoided by processing the data to remove the elastic strain, which leads us to use the inelastic axial strain as our proxy for microstructural state.

Figure 4 shows a synoptic plot of the evolution of the calculated normalized axial and radial *P* wave speed as a function of inelastic axial strain for the same three experiments. The wave speed variations are normalized by the initial wave speed prior to deformation at the appropriate confining pressure. Remarkably, despite the wide range of strain rates (from 10^{-5} s^{-1} down to $6.9\,10^{-8}$ s^{-1}) and the different experimental conditions (imposed constant strain rate or applied stress), the relative change of *P* wave speed is quantitatively very similar for all the tests. This similarity in the evolution of *P* wave speeds with inelastic strain between the three tests implies that the microstructural state of the samples can be considered to be a simple function of the amount of inelastic axial strain.

We note that while we consider this interpretation to be valid over the range of strain rates and stresses investigated here, it will not necessarily be valid for other arbitrary stresses, strains, and strain rates. In general, the constitutive behavior of cracked materials is path dependent, i.e., the stress versus strain response depends on the material's deformation history. This is all the more true since the main micromechanism of deformation is cracking, which is irreversible under the ambient temperature conditions of our tests. Despite these limitations, for the range of stress conditions investigated here, the wave velocity data show that the inelastic strain is an appropriate proxy for the microstructural state of the samples.

4. Energy Deficit and Creep Strain Rates

In the previous section we established that the inelastic axial strain is a relevant proxy for the microstructural state of the samples. In this section we make use of this tool to investigate how the creep strain rate evolution is related to the applied creep stress and to the stress applied (for the same microstructural state) in constant strain rate experiments.
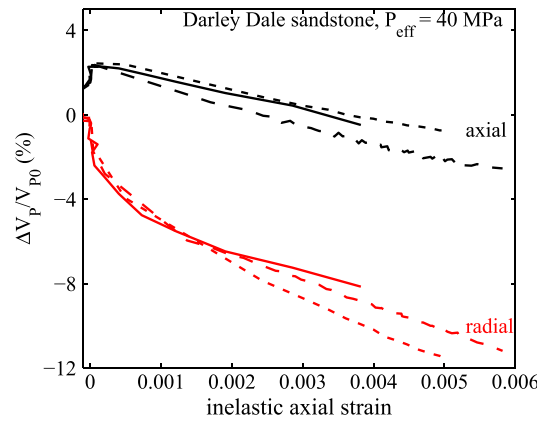
Figure 4. Relative evolution of *P* wave speed along the axis of compression (black) and perpendicular to the axis of compression (red) as a function of the inelastic axial strain. Solid lines correspond to a constant strain rate (10^{-5} s^{-1}) experiment (dd-c2-09), and dashed lines and dotted lines correspond to creep experiments performed under 154.7 MPa (dd-c2-34) and 157.0 MPa (dd-c2-13) differential stress, respectively. The minimum strain rates achieved during the creep tests were $4.5\,10^{-7}$ s^{-1} and $6.9\,10^{-8}$ s^{-1}, respectively. Experiments performed on Darley Dale sandstone under 40 MPa effective pressure.

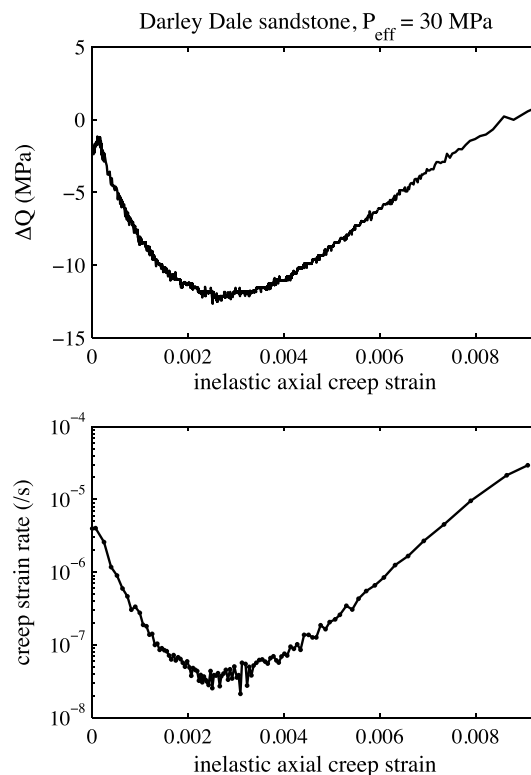## 4.1. Comparison of Creep and Constant Strain Rate Data

Figure 5 shows the differential stress (denoted *Q*) as a function of the inelastic axial strain for one creep experiment (in black) and one constant strain rate experiment (in grey) performed on Darley Dale sandstone at 30 MPa effective pressure. As expected, the behavior is the same during the loading stage, since the imposed condition (constant strain rate of 10^{-5} s^{-1}) is the same. In the creep experiment, once the creep stress is reached, the stress is maintained constant. By contrast, the stress keeps evolving during the constant strain rate experiment. In the latter case, the differential stress first increases until it reaches a peak (around 147 MPa) at 0.005 inelastic axial strain; it then decreases gradually. No macroscopic dynamic stress drop occurred, since the machine stiffness is high enough to prevent runaway deformation in the strain-weakening regime. After 0.01 inelastic strain, the stress applied to the sample under creep conditions

could no longer be maintained as the deformation rate increased dramatically (the sample experienced tertiary creep, see Figure 1).

A striking observation is that the sample deformed under constant stress fails macroscopically (i.e., the deformation rate started to increase in an uncontrollable manner) when the two curves (constant strain rate and constant stress) intersect each other. For the whole range of inelastic strain experienced by the samples in both tests, we can calculate the difference ΔQ between the differential stress applied during creep (which is constant) and the differential stress applied during deformation at constant strain rate. Creep starts at $\Delta Q = 0$ and then becomes negative as the creep stress remains below the stress applied during constant strain rate deformation, and we observe in Figure 5 that creep deformation becomes unstable when the stress difference returns to $\Delta Q = 0$.
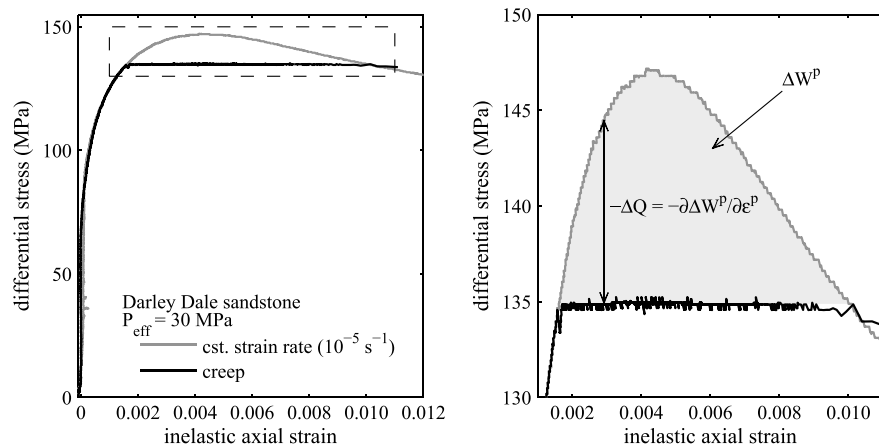
Figure 5. Differential stress versus inelastic axial strain for two samples of Darley Dale sandstone deformed at 30 MPa effective pressure. One sample was deformed at constant strain rate (grey line), and one sample was deformed at constant stress (black line), after a preliminary loading stage at constant strain rate. (right) An expanded view of the portion of the curves marked by the dashed rectangle in the left panel. The grey area corresponds to the strain energy deficit of creep deformation.

AGU **Journal of Geophysical Research: Solid Earth**   10.1002/2013JB010448

Figure 6 shows the evolution of both the stress difference ΔQ and the creep strain rate (on a log scale) as a function of the inelastic axial creep strain. There is a remarkable similarity between the two curves. Several fundamental observations can be made. First, the creep strain rate is never constant, in qualitative agreement with the recent micromechanical model of *Brantut et al.* [2012]. Second, the minimum creep strain rate is achieved when the stress difference is largest (most negative), i.e., when the differential stress is at the peak during the constant strain rate test.

These observations are presented in a more synoptic manner in Figure 7 for all three sandstones tested at 10 MPa effective stress, by directly plotting the creep strain rates (normalized by the constant strain rate of 10^{-5} s^{-1}) as a function of the stress difference. In the graphs of Figure 7, each curve has two branches: one (solid lines) corresponds to decreasing strain rate, and the other one (dotted lines) corresponds to increasing strain rate. The two branches are not perfectly superimposed, and for the case of Bentheim sandstone, the accelerating branch is not straight in the log linear plot. We also note that some curves do not start at $\Delta Q = 0$ at the onset of creep (for a normalized strain rate close to 1). This can be

Figure 6. (top) Stress deficit ΔQ (see Figure 5 for a graphical definition) and (bottom) creep strain rate as a function of the inelastic axial creep strain for Darley Dale sandstone at 30 MPa effective pressure.

attributed to the natural variability between the samples deformed under constant strain rate and creep conditions, which produces a deviation of the stress-strain curves during the loading stage. In other words, the stress-strain curves are not always perfectly superimposed during the loading stage. Nevertheless, we generally observe the following: (1) the minimum strain rate is systematically achieved for the minimum ΔQ; (2) the logarithm of the creep strain rate is proportional to the stress difference (at least in the decreasing
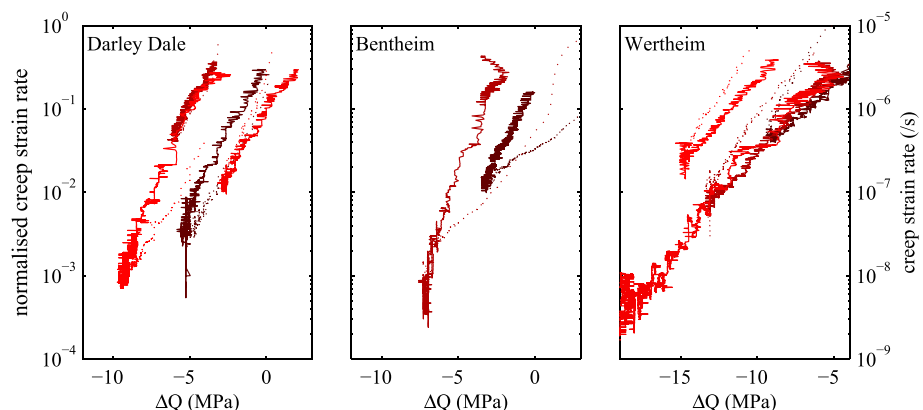
Figure 7. Creep strain rate as a function of the stress difference ΔQ for all three sandstones tested at 10 MPa effective pressure. For each rock type, each shade of red corresponds to one creep experiment, compared to the same reference constant strain rate test (see text for details). The solid lines correspond to the evolution of strain rate and ΔQ before the strain rate reaches its minimum, whereas the dotted lines correspond to the evolution after the minimum strain rate is passed.
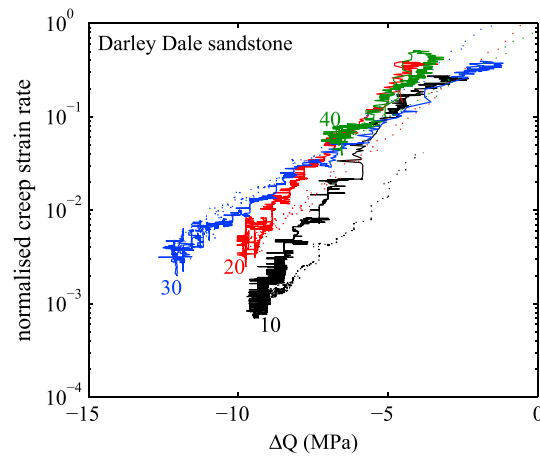
Figure 8. Creep strain rate normalized by a constant strain rate of 10^{-5} s^{-1} as a function of the stress difference ΔQ for a set of experiments performed on Darley Dale sandstone under effective pressures ranging from 10 to 40 MPa.

strain rate branch); and (3) the coefficient of proportionality for the decreasing strain rate branch is well reproducible for a given rock type. These observations can be summarized in the following empirical equation:

$$\dot{\epsilon}_{\text{creep}}/\dot{\epsilon}_0 \approx \exp(\Delta Q/\sigma^*), \qquad (2)$$

where $\dot{\epsilon}_{\text{creep}}$ is the instantaneous brittle creep strain rate, $\dot{\epsilon}_0$ is the strain rate applied during the constant strain rate test (equal to 10^{-5} s^{-1}), and σ^* is a characteristic "activation" stress that gives the stress dependency of the creep strain rate. The activation stress σ^* can be determined from the decreasing strain rate branches of all the available curves and ranges from 1.0 to 1.4 MPa for Darley Dale sandstone, from 0.8 to 1.2 MPa for Bentheim sandstone, and from 2.2 to 2.7 MPa for Wertheim sandstone.

We note that the transition from the decelerating branch to the accelerating branch in Figure 7 is equivalent to the peak stress in a constant strain rate experiment and is therefore also likely to be associated with the onset of localization of deformation onto a fault plane.

4.2. Effect of Confining Pressure
The procedure described above was repeated for a set of experiments performed on Darley Dale sandstone under effective pressures ranging from 10 to 40 MPa. The results are compiled in Figure 8, which again shows the normalized creep strain rate as a function of the stress difference.

The empirical exponential relation between strain rate and stress difference (equation (2)) holds for all the effective pressures investigated. Notably, the activation stress σ^* does not seem to depend upon effective pressure in any systematic manner: σ^* is around 1.0 MPa at $P_{\text{eff}} = 10$ MPa (see above), 1.2 MPa at $P_{\text{eff}} = 20$ MPa, 2.2 MPa at $P_{\text{eff}} = 30$ MPa, and 1.6 MPa at $P_{\text{eff}} = 40$ MPa. These values are within the range determined above for all the sandstones tested at $P_{\text{eff}} = 10$ MPa.

4.3. Energy Deficit
In the previous sections we established a macroscopic, empirical description of time-dependent brittle deformation of the tested sandstones samples: we discovered that the strain rate was an exponential function of the stress deficit and that the confining pressure was apparently not quantitatively influencing this relation. Here we use a thermodynamic approach to understand the origin of our empirical description and what it implies in terms of the energetics of brittle deformation.

The inelastic strain energy (which we define here as the irrecoverable work associated with the inelastic deformation) input to a rock sample under triaxial conditions is

$$W^{\text{p}} = \int_0^{\epsilon_{\text{ax}}^{\text{p}}} Q \, d\epsilon_{\text{ax}}^{\text{p}} + \int_0^{\epsilon_{\text{vol}}^{\text{p}}} P_{\text{eff}} \, d\epsilon_{\text{vol}}^{\text{p}}, \qquad (3)$$

where $\epsilon_{\text{ax}}^{\text{p}}$ is the inelastic axial strain, $\epsilon_{\text{vol}}^{\text{p}}$ is the inelastic volumetric strain, Q is the differential stress, and P_{eff} is the effective confining pressure. Under both constant strain rate and creep conditions, we consider that the inelastic volumetric strain evolution is quantitatively similar (within the natural sample variability and the precision of our experimental equipment; see Appendix A and Figure A1). Hence, for a pair of experiments performed under creep and constant strain rate conditions, we can define an inelastic strain energy difference as

$$\Delta W^{\text{p}} = \int_0^{\epsilon_{\text{ax}}^{\text{p}}} \Delta Q \, d\epsilon_{\text{ax}}^{\text{p}}, \qquad (4)$$

where ΔQ is the stress difference, or stress deficit, defined previously. The inelastic strain energy difference is negative, since ΔQ is negative: thus it corresponds to an energy deficit between the creep and constant strain rate deformation. The absolute value of the energy deficit is shown in Figure 5 (right) as the shaded area between the creep and constant strain rate stress-strain curves. Deformation by brittle creep, at constant applied stress, generally requires less energy than deformation at an imposed (faster) constant strain rate. The energy deficit is likely to correspond to a decreased dissipation in the case of slower, creep deformation: dissipation includes thermal energy generation, friction at grain contacts, and radiation of elastic waves (in the form of acoustic emissions, as shown by *Brantut et al.* [2013a]).

From equation (4) we note that the inelastic strain energy difference ΔW^p is simply the integral of the stress difference ΔQ; in other words,

$$\Delta Q = \frac{\partial \Delta W^p}{\partial \epsilon_{ax}^p}. \tag{5}$$

Hence, the stress difference simply corresponds to a difference in energy release rate per unit of inelastic axial strain. If we formally introduce an internal state variable H, which symbolically encapsulates the microstructural state of the rock [see *Rice*, 1975], then we can rewrite ΔQ as follows:

$$\Delta Q = \frac{\partial H}{\partial \epsilon_{ax}^p} \frac{\partial \Delta W^p}{\partial H}, \tag{6}$$

where $\partial \Delta W^p / \partial H$ is the difference in strain energy release rate per unit of internal state variable H and $\partial H / \partial \epsilon_{ax}^p$ is the change of state H per unit of inelastic axial strain. The definition of $\partial \Delta W^p / \partial H$ is analogous to a difference in fracture energy release rate. More precisely, if H is viewed as an average microcrack length within the sample, then $\partial \Delta W^p / \partial H$ is simply the difference between the average fracture energy release rates between the pair of rock samples [*Rice*, 1975]. In that case, $\partial H / \partial \epsilon_{ax}^p$ simply corresponds to the rate of crack extension per unit of inelastic axial strain.

In section 3 we showed how the inelastic axial strain is a well-defined, monotonic function of the microstructural state, which we have now formally introduced as an internal state variable H. If we denote

$$H' = \frac{\partial H}{\partial \epsilon_{ax}^p}, \quad \text{and} \tag{7}$$

$$\Delta W^{p'} = \frac{\partial \Delta W^p}{\partial H}, \tag{8}$$

then we can recast the empirical relation between creep strain rate and stress difference as

$$\frac{\dot{H}_{creep}}{\dot{H}_0} \approx \underbrace{\frac{[\partial \epsilon_{ax}^p / \partial H]_0}{[\partial \epsilon_{ax}^p / \partial H]_{creep}}}_{\approx 1} \exp\left(\frac{H' \Delta W^{p'}}{\sigma^*}\right). \tag{9}$$

In equation (9), $\dot{H}_{creep}$ and $\dot{H}_0$ denote the evolution of the internal state variable H with time under constant stress (creep) and constant strain rate conditions, respectively. The prefactor of the exponential should be close to 1 since we have already established that the inelastic axial strain is a good measure of the internal microstructural state of the samples and in particular the cracking state (Figure 4). Considering that $\dot{H}$ is analogous to a crack growth rate (i.e., it is a rate of change of the internal state), relation (9) is then analogous to well-known subcritical crack growth laws, which are of the form [e.g., *Freiman*, 1984; *Wan et al.*, 1990]

$$v \propto \exp\left(-\frac{bK}{RT}\right), \quad \text{or} \tag{10}$$

$$v \propto \exp\left(-\frac{b'G}{RT}\right), \tag{11}$$

where v is the crack growth rate, R is the gas constant, T is the absolute temperature, G is the fracture energy at the crack tip, K is the stress intensity factor at the crack tip (generally mode I), and b and b' are constitutive parameters describing the sensitivity of the crack growth rate to K and G, respectively.

The comparison between equations (9) and (11) indicates that the activation stress σ^* should reflect the parameter b'/RT, which gives the sensitivity of crack growth rate to variations in crack tip energy release rate. Because the stress intensity factor K is a linear function of the applied stresses, the same observation can be made (b'/RT being replaced by b/RT) if we compare equations (2) and (10). These analogies also shows that the activation stress is a combination of the subcritical cracking parameters and a term (e.g., H') linking the internal state evolution (e.g., crack length) to the macroscopically averaged quantity (here, inelastic strain).

Despite the generality of our approach, the practical use of a relation like (9) is limited by our poor knowledge, in practice, of the correct general meaning of H. Hence, the precise relation between $\Delta W^{p'}$ and, say, the actual energy release rate of the microcracks within the rock sample is poorly constrained.

5. Extraction of Microscale Processes

In the previous section we established an empirical exponential relation between strain rate and stress deficit during creep deformation and showed that such a relation should be linked to small-scale subcritical crack growth laws. In this section we develop a more specific framework, based on fracture mechanics, which will allow us to determine precisely a link between the macroscopic stress dependency parameter of creep strain rate (the activation stress σ^*) and microscale subcritical crack growth parameters.

5.1. Empirical Micromechanical Functions

One way to determine a precise link between the activation stress σ^* and the subcritical crack growth parameter b is to make several assumptions as regards the micromechanics of brittle deformation. In brittle materials, a common method to establish macroscopic stress-strain relations from microscale processes is to assume that deformation is only due to microcrack closure, sliding, and growth [see *Paterson and Wong*, 2005, chap. 6]. Further assuming that the solid matrix of the rock remains purely elastic, the crack growth criterion can be written in terms of the stress intensity factor, calculated from Linear Elastic Fracture Mechanics (LEFM). At the microscopic level, microcrack growth is mostly in mode I, since cracks that nucleate in other modes do not grow in their own planes and quickly become pure mode I cracks aligned with the maximum principal stress [e.g., *Nemat-Nasser and Horii*, 1982]. Following LEFM, a generic form for the mode I stress intensity factor, denoted K_I, in triaxial conditions, is

$$\frac{K_I}{\sqrt{\pi c}} = \alpha(l)Q + \beta(l)P_{\text{eff}}, \qquad (12)$$

where c is a characteristic microcrack or flaw length (generally commensurate with the grain size) and $\alpha(l)$ and $\beta(l)$ are two nonlinear functions of the mode I microcrack size l. The expression for K_I in (12) is in terms of macroscopically applied stresses Q and P_{eff}, and hence it effectively corresponds to an averaged, representative K_I. Such an expression would be rigorously exact if all the microcracks had the same size and geometry.

In conventional micromechanical approaches, one makes precise assumptions about the microcrack geometry with respect to the applied stresses, and explicit formulations of the functions $\alpha(l)$ and $\beta(l)$ can then be established. This is the case, for instance, in the "wing crack" model of *Ashby and Sammis* [1990] for triaxial conditions (further developed for generalized stress states by *Deshpande and Evans* [2008]; *Bhat et al.* [2011]). However, the assumptions about the crack size and geometry are generally very restrictive; even then, some simplifications have to be made in order to access analytical formulations of K_I in terms of crack length and stresses. Such "ab initio" micromechanical models are complex and need the introduction of numerous, sometimes poorly constrained, microscopic parameters.

Here we adopt a different approach, based directly on experimental data. Instead of looking for a simplified, tractable microcrack geometry, we will attempt to determine in the most direct way the functions $\alpha(l)$ and $\beta(l)$ by inverting experimental data.
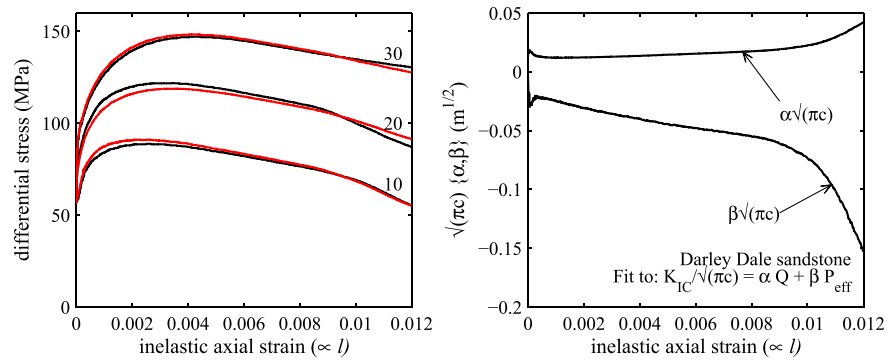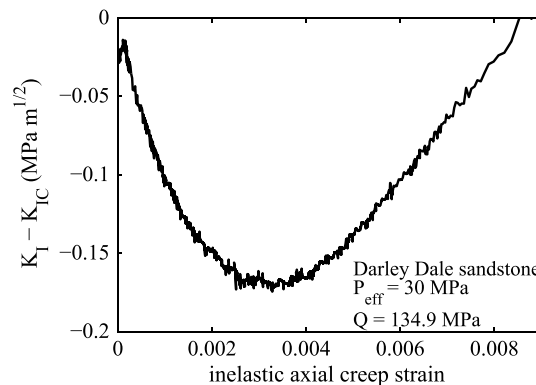
Figure 9. (left) Differential stress as a function of inelastic axial strain for Darley Dale sandstone samples deformed at constant strain rate (10^{-5} s^{-1}), for effective pressures ranging from 10 to 30 MPa (numbers indicated on the curves). Experimental data are shown in black, and least squares fits to equation (12) with $K_I = K_{IC} = 1$ MPa m$^{-1/2}$ are shown in red. (right) Corresponding evolution of $\alpha\sqrt{\pi c}$ and $\beta\sqrt{\pi c}$ with inelastic axial strain.

5.2. Determination of K_I Evolution

In order to determine the evolution of an effective K_I during the experiments, we need to invert for the evolution of α and β at all stages (i.e., as a function of an effective microcrack length l) throughout deformation. Here again we make use of the observation that inelastic axial strain is a reasonable proxy for the microstructural state of the samples, where microstructural state is now identified relative to an effective crack length l.

We now consider that, during the deformation tests performed at a constant strain rate of 10^{-5} s^{-1}, the imposed deformation is so fast that the microcracks grow at speeds much higher than the typical sub-critical crack growth rates, and therefore the crack growth criterion is essentially determined by the time-independent fracture toughness. Equivalently, we can also consider that an imposed deformation rate induces a constant crack growth rate and therefore that K_I remains constant during such tests. In all cases, we assume that the effective stress intensity factor is close to the fracture toughness of the material (K_{IC}) for the samples deformed at constant ("fast," 10^{-5} s^{-1}) strain rate. K_{IC} is a material constant, equal to 1 MPa m$^{1/2}$ for pure quartz in wet conditions [*Atkinson*, 1984]. Using this constant value for K_I in equation (12), we see that the functions $\alpha\sqrt{\pi c}$ and $\beta\sqrt{\pi c}$ can be obtained as functions of the inelastic axial strain by inverting the evolution of differential stress Q at various effective pressures P_{eff} during constant strain rate tests. The inversion is performed by a least squares method on the data obtained at $P_{eff} = 10$, 20, and 30 MPa. The fits are shown for Darley Dale sandstone in Figure 9 (left), and the resulting *empirical micromechanical functions* $\alpha\sqrt{\pi c}$ and $\beta\sqrt{\pi c}$ are shown in Figure 9 (right).

The function α, which corresponds to the effect of differential stress (i.e., a measure of the average shear stress) on the effective stress intensity factor, is always positive: as expected, larger differential stress tend to increase K_I at crack tips. During deformation, α remains almost constant, only increasing slightly at inelastic strain larger than 1%. The function β, which quantifies the effect of effective pressure on the effective stress intensity factor, is always negative: this is also expected, since larger confining pressures tend to close cracks and decrease K_I. β decreases continuously with increasing inelastic deformation. This is also consistent with basic fracture mechanics concepts: large cracks tend to be easier to close (i.e., K_I is more sensitive to closing stresses).

Figure 10. K_I deficit as a function of inelastic axial creep strain for a Darley Dale sandstone (sample dds13 in Table 1) deformed under creep conditions.

We are now in possession of an *empirical micromechanical model* which allows us to link an effective stress intensity factor to the
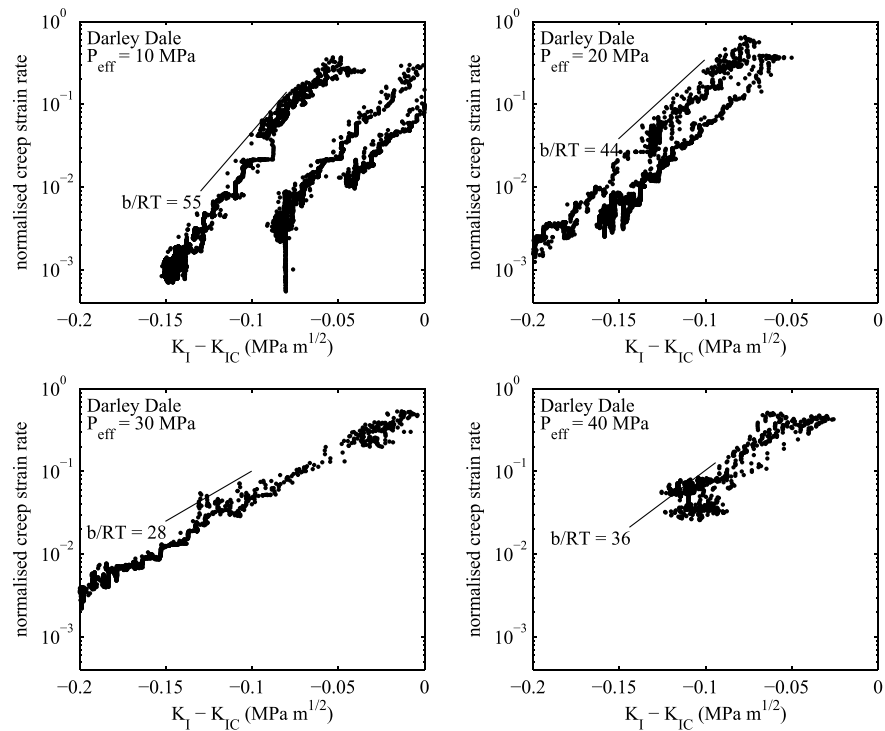
Figure 11. Normalized creep strain rate as a function of $K_I - K_{IC}$ for Darley Dale sandstone experiments performed at P_{eff} ranging from 10 to 40 MPa. Only the data from the onset of creep to the minimum strain rate were used.

applied stresses and to a microscopic state variable (here, an effective crack length, which is well reflected by the inelastic axial strain). Using the inverted values of the functions α and β, we are then able to apply the model to our creep experiments, during which the effective stress intensity factor is not constant. Specifically, we can relate the stress deficit ΔQ to a difference between the creep stress intensity factor and the fracture toughness (or a "K_I deficit"):

$$K_I - K_{IC} = \alpha(l)\sqrt{\pi c}\Delta Q. \tag{13}$$

Since the factor $\alpha(l)\sqrt{\pi c}$ remains almost constant for inelastic deformation below 1% (see Figure 9), the K_I deficit is in fact approximately proportional to the stress deficit. Therefore, the evolution of the effective $K_I - K_{IC}$ with inelastic strain, shown in Figure 10, actually mirrors the evolution of ΔQ, which is shown in Figure 6. This evolution is qualitatively similar to that obtained by *Brantut et al.* [2012] from a theoretical micromechanical model, in which an analytical expression for $\alpha(l)$ and $\beta(l)$ was used (based on the wing crack geometry of *Ashby and Sammis* [1990]). The initial decrease in K_I in Figure 10 can be attributed to the progressive crack extension under overall compressive stress, up to the point where microcrack interactions become dominant and any further crack extension produces an increase in K_I.

The relation between the normalized creep strain rate and $K_I - K_{IC}$ is shown in Figures 11 and 12 for the available data on Darley Dale sandstone and Bentheim sandstone, respectively. In these Figures, the strain rate data beyond the minimum strain rate (i.e., beyond the peak stress in the constant strain rate experiments) have been omitted to emphasize the portion of the experiments during which the strain is not yet localized along a fault plane (and hence is more representative of an effective stress intensity factor and crack size).

5.3. Interpretation
As shown and discussed in section 3, the inelastic strain is a simple function of the microstructural state (see Figure 4), and we neglect the load-path dependence of the constitutive response of the material. In that framework, the normalized creep strain rate (ratio of creep strain rate to the reference constant strain rate) is simply proportional to the ratio of crack growth rates of the creep and constant strain rate experiments. Hence, the graphs in Figures 11 and 12, obtained under conditions of triaxial compression, are equivalent to the $K_I - v$ curves that have been obtained in tensile single crack tests [e.g., *Atkinson*, 1984].
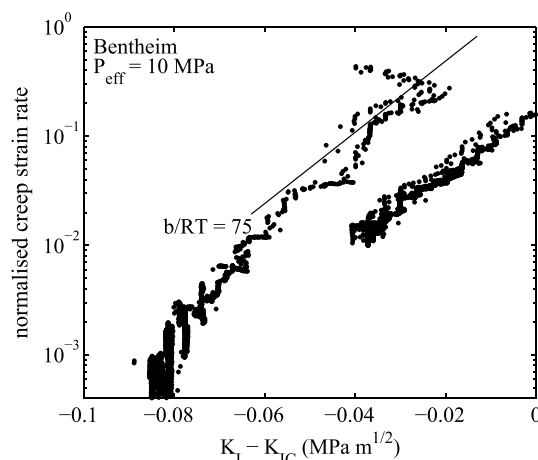
Figure 12. Normalized creep strain rate as a function of $K_I - K_{IC}$ for Bentheim sandstone experiments performed at $P_{eff} = 10$ MPa. Only the data from the onset of creep to the minimum strain rate were used.

Using the subcritical crack growth relation given by *Freiman* [1984],

$$v \propto \exp\left(-\frac{bK_I}{RT}\right), \qquad (14)$$

we determine the values of the parameter b/RT by calculating the average slope of the curves in the log linear plots of Figures 11 and 12. The factor b/RT (in units of $MPa^{-1}m^{-1/2}$) ranges from 28 to 55 for Darley Dale sandstone and is 75 for the available Bentheim sandstone data. There does not seem to be any consistent trend with effective confining pressure: this is entirely as expected, since equation (13) indicates that confining pressure does not play any role in the relation between the stress deficit and the difference in stress intensity factors. This arises because the contribution of confining pressure is the same in both the creep and constant strain rate tests, so that using the stress deficit suppresses the explicit pressure dependence. The range of variation of b/RT can be attributed to the accumulated errors in the data processing: inversion of α and β, processing to obtain inelastic strain, and offsets in stresses due to sample variability.

Based on reaction rate theory, *Wiederhorn et al.* [1980] and *Freiman* [1984] expressed the subcritical cracking parameter b as

$$b = (\pi d)^{-1/2}\Delta V^{\ddagger}, \qquad (15)$$

where d is a length scale that depends on the crack tip structure (which can be approximated to the crack tip radius of curvature) and $\Delta V^{\ddagger}$ is the activation volume of the chemical reaction producing crack growth (for quartz, most likely stress corrosion; see [*Atkinson*, 1984]). Choosing a d value of the order of 1 nm, combined with the b values determined from the experimental data, we calculate activation volumes ranging from 3.9×10^{-6} to 10.5×10^{-6} m^3 mol^{-1}. These values are of the same order of magnitude as the molar volume of quartz, which is consistent with the concept of stress corrosion by local hydrolysis of SiO bonds at crack tips. In addition, despite the relative scatter between experiments, this range is clearly compatible with documented activation volumes for stress corrosion reactions (e.g., around 2×10^{-6} m^3 mol^{-1} for stress corrosion of soda-lime glass in water [*Freiman*, 1984]).

6. Discussion and Implications

6.1. A General Method of Analysis: Empirical Micromechanical Functions
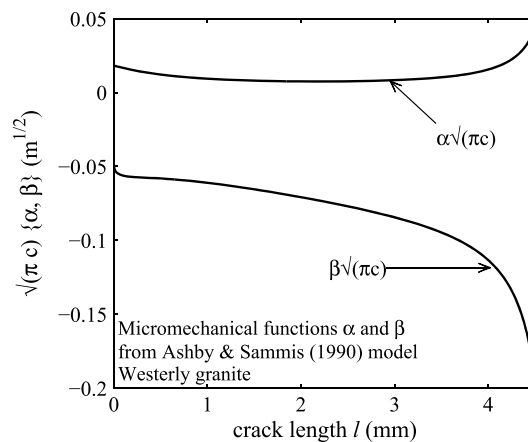
In section 5.2, we established a general methodology that allows the determination of an effective K_I throughout a deformation test, *using only macroscopic observations*. The application of this method requires that there exists an appropriate macroscopically measurable proxy for crack length (in our case, inelastic axial strain) in order to make meaningful comparisons between tests conducted under different conditions. Then, the only assumption required is that fast deformation occurs with $K_I \approx K_{IC}$ at microcrack tips. If at least two stress-strain curves are available for two different effective pressures, the empirical micromechanical functions can be determined using relation (12).

This method of analysis, which relies on LEFM, allows the determination of an empirical micromechanical model with a minimal number of assumptions and only one parameter, K_{IC}, which is a well-documented material property [see, for instance, *Atkinson and Meredith*, 1987]. Hence, we can bypass the mathematical complexities and the large number of assumptions or loosely constrained parameters needed for the development of ab initio micromechanical models, such as those of *Costin* [1985] or *Ashby and Sammis* [1990]. As a point of comparison, however, we can compute the functions α and β given by the model of *Ashby and Sammis* [1990] and compare them with our experimentally derived values. The exact expressions for α and β can be found in Appendix B. Unfortunately, this model cannot be fitted to porous rocks such as Darley Dale sandstone [see *Baud et al.*, 2013]; hence, we can only draw qualitative comparisons by choosing

Figure 13. Evolution of micromechanical functions $\alpha\sqrt{\pi c}$ and $\beta\sqrt{\pi c}$ as a function of the crack length l for the wing crack model of *Ashby and Sammis* [1990] (see Appendix B for details). Parameter values are given in Appendix B and correspond to Westerly granite.

a rock type for which the model is applicable. For that purpose, we choose parameter values relevant to Westerly granite, which can be found in *Brantut et al.* [2012] (see Appendix B). Figure 13 shows the evolution of $\alpha\sqrt{\pi c}$ and $\beta\sqrt{\pi c}$ as functions of the crack length l. Both functions evolve in a manner remarkably similar to those inverted from our experimental data (Figure 9, right). Furthermore, the numerical values derived from the model and from the experiments are within the same range, even though the parameter values in the model do not correspond to the same rock type. This strong similarity between the results from processing our experimental data and ab initio approaches, such as the wing crack model of *Ashby and Sammis* [1990], reinforces our approach. This qualitative comparison exercise should be complemented with a more systematic quantitative analysis. However, such an

analysis is beyond the scope of this study but could be performed using experimental data for Westerly granite or any other appropriate rock type.

Our overall methodology is unfortunately only approximate, because it implicitly assumes that the loading path dependence of the constitutive behavior can be neglected. Hence, it can be used only to compare tests performed under similar stress conditions. This is legitimate in the context of brittle creep, because the initial loading of the sample is always the same, and the constant applied stress in the creep tests remains close to the applied stress in the constant strain rate tests (for the same inelastic axial strain). Further developments are needed to explore how path dependence affects the results obtained from experiments performed under significantly different conditions. In other words, using our functions α and β determined from triaxial constant strain rate tests to predict the behavior under generalized loading configurations (e.g., true triaxiality) might result in serious bias.

6.2. A "Rate-and-State" Deformation Law for Brittle Rocks

Under upper crustal conditions, where water is ubiquitous as a pore fluid, even brittle rock deformation driven entirely by crack growth is time dependent due to chemically assisted subcritical crack growth. As documented above, time-dependent crack growth results in rate-dependent brittle deformation. Rate dependency in the brittle regime has also been widely documented for frictional sliding along preexisting interfaces or fault gouges [e.g., *Scholz*, 2002]. A common mathematical description of such rheologies is in the form of rate-and-state friction laws, where the coefficient of friction depends logarithmically on slip rate and on a set of internal state variables [e.g., *Rice*, 1983]. In general, rate-and-state friction laws can be written as [*Nakatani*, 2001]

$$v(\tau, \theta) = v_0 \exp\left(\frac{\tau - \tau_0(\theta)}{a\sigma}\right), \tag{16}$$

where v is the slip rate, τ is the applied shear stress on the interface, θ is a state variable (or a set of state variables), v_0 is a reference slip rate, σ is the normal stress acting across the fault, a is a constitutive parameter quantifying the stress sensitivity of slip rate, and $\tau_0(\theta)$ is a reference shear stress, which is a function of the state variable(s). In fact, $\tau_0(\theta)$ is the shear stress required to slide the interface at the reference (constant) slip rate v_0. The parallel between the friction law (16) and the relation (2) we determined empirically for brittle creep deformation of intact rock is evident. The axial strain rate in relation (2) is analogous to the sliding velocity in relation (16), the differential stress deficit ΔQ is analogous to the shear stress difference $\tau - \tau_0(\theta)$, and the activation stress σ^* is analogous to the product $a\sigma$. In this respect, our empirical formulation (equation (2)) is a type of "rate-and-state" deformation law for intact materials. Within this empirical framework, the analogue of "state" is then simply the inelastic axial strain: the stress needed to deform

the rock at a constant reference velocity (analogue to $\tau_0(\theta)$ in a friction law) has indeed been shown to be a function of (primarily) inelastic strain, which reflects the "internal microstructural state" of the rock (see section 3).

From a microscopic point of view, we have seen in the previous section that the exponential dependency of strain rate upon stress deficit only arises because the micromechanical function $\alpha(l)\sqrt{\pi c}$ remains essentially constant with inelastic strain (or, in our assumption, effective microcrack length; see Figure 9). Combining expressions (13) and (15), the activation stress σ^* can then be expressed as

$$\sigma^* \approx \frac{RT\sqrt{d/c}}{\langle\alpha\rangle\Delta V^{\ddagger}}, \tag{17}$$

where $\langle\alpha\rangle$ is the average value of the function $\alpha(l)$. In rate-and-state friction laws, the parameter $a\sigma$ (analogous to our σ^*) can be expressed from reaction rate theory as [e.g., *Nakatani*, 2001; *Rice et al.*, 2001]

$$a\sigma = \frac{RT\sigma}{\Omega\sigma_c}, \tag{18}$$

where Ω is the activation volume of the physical (or chemical) process responsible for sliding at asperities and σ_c is the local stress acting on the microscale asperities. Using typical values for a obtained from experimental data, *Rice et al.* [2001] determined activation volumes Ω of the order of the molar volume of quartz. This clearly parallels our results for $\Delta V^{\ddagger}$. Whether the microscale, thermally activated process responsible for rate-dependent friction is actually the same as the one responsible for subcritical cracking (for quartz, most likely stress corrosion reactions) remains unclear. This discussion goes far beyond the scope of this paper, and extensive future work on this subject is needed to investigate if this parallel between time-dependent friction and time-dependent deformation of intact rock results from a common physical mechanism.

Nevertheless, the semiempirical formulation (2) can be seen as a useful description of the rate dependency of deformation in the brittle regime. This relation is also directly comparable to that of *Lockner* [1998], which was determined for Westerly granite based on the most complete data set existing for a single rock type. *Lockner* [1998] included an explicit, empirical description for the nonlinearity of the stress-strain behavior at constant strain rate (i.e., our reference curves at 10^{-5} s^{-1}). In our analysis, we bypass this issue by introducing the concept of stress deficit. Our methodology allows for a very simple treatment of the time dependency, which can be applied routinely to typical triaxial experiments. The determination of the activation stress only requires two experiments: one at fast, constant strain rate and one under constant stress conditions (at the same effective pressure). Then, once σ^* is known, equation (2) can be used to make reasonable predictions of times to failure and creep strain rates. Note that the only major problem with using this method for making predictions is that sample variability can significantly offset the strain rates and hence the time to failure, as shown for instance in Figure 6. The problem of sample variability, or, equivalently, the variability in initial microstructural state [see *Brantut et al.*, 2013b], remains the main issue for precise predictions in natural materials such as rocks.

The validity of equation (2) for strength predictions under different imposed constant strain rates could potentially be checked against triaxial data obtained over a range of strain rates. If applied to estimate the strength (or, more precisely, the stress deficit) of a rock under deformation at constant strain rates slower than the reference strain rate (10^{-5} s^{-1}), equation (2), according to our estimates for σ^*, would predict a decrease in strength of a few megapascals per decade of strain rate. Again, because of natural sample variability, such small variations in strength would be rather difficult to observe consistently in a data set obtained at different imposed constant strain rates. A more reliable methodology would be to perform strain rate steps during tests, similarly to the velocity steps typically performed during friction experiments. Such an approach will be tested and assessed in future work.

7. Conclusions

We performed triaxial experiments on three types of sandstone and compared the results obtained under constant strain rate (10^{-5} s^{-1}) and creep (constant stress) conditions. The evolution of P wave speeds as a function of inelastic axial strain is the same in both types of test, despite differences in strain rates of up to 3 orders of magnitude. This similarity indicates that inelastic axial strain is an appropriate proxy for the microstructural state of the samples, under both creep and constant strain rate conditions.
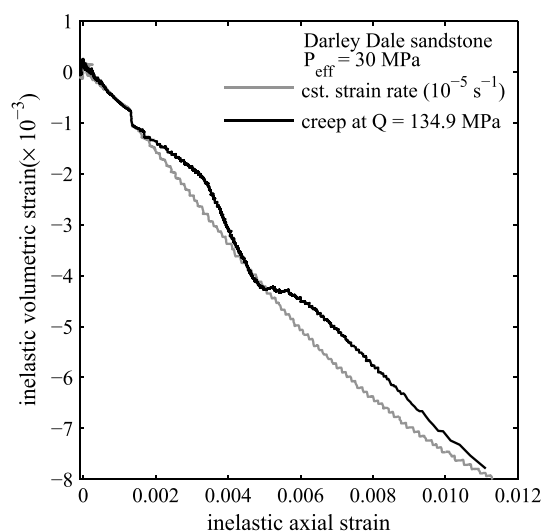
Figure A1. Inelastic volumetric strain as a function of inelastic axial strain for a creep test (in black) and a constant strain rate test (in grey) performed at 30 MPa effective pressure.

The comparison of differential stress versus inelastic strain curves for both types of test reveals that creep deformation requires less mechanical work to bring the sample to failure. This energy deficit corresponds to a stress deficit, which can be related to a deficit in energy release rate for the cracks, or, equivalently, to a deficit in crack tip stress intensity factors. The evolution of strain during creep tests is well described, empirically, by an exponential of the stress deficit. This description introduces an activation stress σ^* that can be easily quantified by measuring the slope of the logarithm of strain rate versus stress deficit curves. An interesting particular consequence of these observations is that the creep strain rate is in fact *never* constant. The so-called secondary creep stage is simply an inflection period, during which strain rate remains close to or at its minimum for an extended period of time.

Based on linear fracture mechanics, and the assumption that crack growth is the dominant deformation mechanism, we developed a method to estimate the evolution of an effective stress intensity factor at crack tips during creep deformation. The estimated evolution mirrors the evolution of the stress deficit. Further assuming that the relation between crack size and inelastic strain rate is approximately linear before peak stress is reached, we determined a relation between crack growth rate v and stress intensity factor K_I. By analyzing the slope of those $K_I - v$ curves using the stress corrosion law of *Freiman* [1984], we determined an activation volume for the stress corrosion reaction responsible for brittle creep in our samples. This activation volume is of the same order of magnitude as the molar volume of quartz and is close to the activation volumes determined independently from typical subcritical crack growth tests [*Freiman*, 1984].

The exponential relation between strain rate and stress deficit determined for brittle deformation of intact rocks has the same form as rate-and-state friction laws which relate slip rate to applied shear stress on an interface. The stress dependency of slip rate in rate-and-state friction laws arises from thermally activated processes [e.g., *Nakatani*, 2001; *Rice et al.*, 2001] which have an activation volume very similar to the one determined in our analysis for stress corrosion cracking. This similarity opens the way for further studies aimed at establishing the precise the relation between fracture of intact rocks and friction along rock interfaces.

Appendix A: Volumetric Strain Evolution

Here we compare the evolution of inelastic volumetric strain as a function of inelastic axial strain for both constant strain rate and creep experiments. The inelastic volumetric strain was calculated from the porosity change of the samples (measured with a pore volumometer), corrected from the drained modulus estimated in the elastic part of the differential stress versus volumetric strain behavior. Figure A1 shows the inelastic volumetric strain as a function of inelastic axial strain for two experiments performed on Darley Dale sandstone at 30 MPa effective pressure, under constant strain rate (grey) and creep (black) conditions. The evolution is remarkably similar between the two experimental conditions. For the case of creep, the volumetric strain oscillates near the reference curve of the constant strain rate experiment. This oscillation can be attributed to thermal effects (the experiment was conducted over several days). These thermal effects affect most of our creep data and cannot be easily corrected. For the purpose of this study, we consider therefore that the inelastic volumetric strain does not significantly differ from one test to another when the effective pressure conditions are the same.

Appendix B: Wing Crack Model

In the approach of *Ashby and Sammis* [1990], rocks are modeled as an elastic material containing initial flaws oriented at 45° from the axis of compression. Under increasing differential stress, the flaws extend and generate "wing" cracks, which are mode I cracks oriented parallel to the axis of compression. Interactions between cracks is taken into account in a global manner, by balancing the crack extension force and the force exerted by confining pressure onto the uncracked ligaments between the wing crack elements. In this approach, the internal state parameter can be identified to the wing crack length (or, equivalently, the wing crack density). The details of the approach and calculations are not reported here, and readers are referred to *Ashby and Sammis* [1990], *Deshpande and Evans* [2008], *Bhat et al.* [2011], and *Brantut et al.* [2012] for developments on the subject. The mode I stress intensity factor at the tips of the wing cracks is expressed as [*Ashby and Sammis*, 1990]

$$\frac{K_{\mathrm{I}}}{\sqrt{\pi c}} = \left(A_1 Q + (A_1 - A_3)P_{\mathrm{eff}}\right)\left(c_1(l) + c_2(l)\right) - c_3(l)P_{\mathrm{eff}}, \tag{B1}$$

where

$$A_1 = \pi\sqrt{\frac{B}{3}}\left(\sqrt{1+\mu^2} + \mu\right), \quad A_3 = A_1\frac{\sqrt{1+\mu^2} + \mu}{\sqrt{1+\mu^2} - \mu},$$
$$c_1(l) = \pi^{-2}(l/c + B)^{-3/2},$$
$$c_2(l) = 2(\pi\gamma)^{-2}(l/c)^{1/2}/\left[\rho_0^{-2/3} - (1 + l/(\gamma c))^2\right],$$
$$c_3(l) = (2/\pi)(l/c)^{1/2}.$$

In the preceding equations, l is the wing crack length, B is a nondimensional factor, μ is the friction coefficient on the initial flaws, $\gamma = \sin(45°)$, and ρ_0 is the initial flaw density. For Westerly granite, the parameter values are as follows [*Brantut et al.*, 2012]: $B = 1.1459$, $\mu = 0.7$, $\rho_0 = 0.0028$, and the initial flaw size is $c = 1.1$ mm. From equation (B1) we obtain the following expressions for $\alpha(l)$ and $\beta(l)$:

$$\alpha(l) = A_1\left(c_1(l) + c_2(l)\right), \tag{B2}$$
$$\beta(l) = (A_1 - A_3)\left(c_1(l) + c_2(l)\right) - c_3(l). \tag{B3}$$

References

Ashby, M. F., and C. G. Sammis (1990), The damage mechanics of brittle solids in compression, *Pure Appl. Geophys.*, *133*(3), 489–521.
Atkinson, B. K. (1984), Subcritical crack growth in geological materials, *J. Geophys. Res.*, *89*(B6), 4077–4114.
Atkinson, B. K., and P. G. Meredith (1987), The theory of subcritical crack growth with applications to minerals and rocks, in *Fracture Mechanics of Rock*, edited by B. K. Atkinson, pp. 111–116, Academic Press, London.
Ayling, M. R., P. G. Meredith, and S. A. F. Murrell (1995), Microcracking during triaxial deformation of porous rocks monitored by changes in rock physical properties, I. Elastic-wave velocity measurements on dry rocks, *Tectonophysics*, *245*, 205–221.
Baud, P., and P. G. Meredith (1997), Damage accumulation during triaxial creep of Darley Dale sandstone from pore volumometry and acoustic emission, *Int. J. Rock Mech. Min. Sci.*, *34*(3–4), 371.
Baud, P., V. Vajdova, and T.-F. Wong (2006), Shear-enhanced compaction and strain localization: Inelastic deformation and constitutive modeling of four porous sandstones, *J. Geophys. Res.*, *111*, B12401, doi:10.1029/2005JB004101.
Baud, P., S. Vinciguerra, C. David, A. Cavallo, E. Walker, and T. Reuschlé (2009), Compaction and failure in high porosity carbonates: Mechanical data and microstructural observations, *Pure Appl. Geophys.*, *166*, 869–898.
Baud, P., T.-F. Wong, and W. Zhu (2013), Effects of porosity and crack density on the compressive strength of rocks, *Int. J. Rock Mech. Min. Sci.*, doi:10.1016/j.ijrmms.2013.08.031, in press.
Bhat, H. S., C. G. Sammis, and A. J. Rosakis (2011), The micromechanics of Westerly granite at large compressive loads, *Pure Appl. Geophys.*, *168*(12), 1–18.
Brantut, N., A. Schubnel, and Y. Guéguen (2011), Damage and rupture dynamics at the brittle-ductile transition: The case of gypsum, *J. Geophys. Res.*, *116*, B01404, doi:10.1029/2010JB007675.
Brantut, N., P. Baud, M. J. Heap, and P. G. Meredith (2012), Micromechanics of brittle creep in rocks, *J. Geophys. Res.*, *117*, B08412, doi:10.1029/2012JB009299.
Brantut, N., P. Baud, M. J. Heap, and P. G. Meredith (2013a), Mechanics of time-dependent deformation in crustal rocks, in *Poromechanics V*, edited by C. Hellmich, B. Pichler, and D. Adam, pp. 407–414, American Society of Civil Engineers, Vienna, Austria, doi:10.1061/9780784412992.048.
Brantut, N., M. J. Heap, P. G. Meredith, and P. Baud (2013b), Time-dependent cracking and brittle creep in crustal rocks: A review, *J. Struct. Geol.*, *52*, 17–43.
Costin, L. S. (1985), Damage mechanics in the post-failure regime, *Mech. Mat.*, *4*, 149–160.

David, E. C., N. Brantut, A. Schubnel, and R. W. Zimmerman (2012), Sliding crack model for nonlinearity and hysteresis in the uniaxial stress-strain curve of rock, *Int. J. Rock Mech. Min. Sci.*, *52*, 9–17.

Deshpande, V. S., and A. G. Evans (2008), Inelastic deformation and energy dissipation in ceramics: A mechanism-based constitutive model, *J. Mech. Phys. Solids*, *56*, 3077–3100.

Eccles, D., P. R. Sammonds, and O. C. Clint (2005), Laboratory studies of electrical potential during rock fracture, *Int. J. Rock Mech. Min. Sci.*, *42*(7–8), 933–949.

Fortin, J., Y. Guéguen, and A. Schubnel (2007), Effects of pore collapse and grain crushing on ultrasonic velocities and v_p/v_s, *J. Geophys. Res.*, *112*, B08207, doi:10.1029/2005JB004005.

Freiman, S. W. (1984), Effects of chemical environments on slow crack growth in glasses and ceramics, *J. Geophys. Res.*, *89*(B6), 4072–4076.

Heap, M. J., P. Baud, P. G. Meredith, A. F. Bell, and I. G. Main (2009), Time-dependent brittle creep in Darley Dale sandstone, *J. Geophys. Res.*, *114*, B07203, doi:10.1029/2008JB006212.

Klein, E., and T. Reuschlé (2004), A pore crack model for the mechanical behaviour of porous granular rocks in the brittle deformation regime, *Int. J. Rock Mech. Min. Sci.*, *41*(6), 975–986.

Kranz, R. L. (1979), Crack growth and development during creep in Westerly granite, *Int. J. Rock Min. Mech. Sci.*, *16*, 23–35.

Kranz, R. L (1980), The effects of confining pressure and stress difference on static fatigue of granite, *J. Geophys. Res.*, *85*(B4), 1854–1866.

Kranz, R. L., W. J. Harris, and N. L. Carter (1982), Static fatigue of granite at 200°C, *Geophys. Res. Lett.*, *9*(1), 1–4.

Lockner, D. A. (1998), A generalized law for brittle deformation of Westerly granite, *J. Geophys. Res.*, *103*(B3), 5107–5123.

Nakatani, M. (2001), Conceptual and physical clarification of rate and state friction: Frictional sliding as a thermally activated rheology, *J. Geophys. Res.*, *106*(B7), 13,347–13,380.

Nemat-Nasser, S., and H. Horii (1982), Compression-induced nonplanar crack extension with application to splitting, exfoliation, and rockburst, *J. Geophys. Res.*, *87*(B8), 6805–6821.

Paterson, M. S., and T. F. Wong (2005), *Experimental Rock Deformation—The Brittle Field,* 2nd ed., Springer-Verlag, Berlin Heidelberg.

Rice, J. R. (1975), Continuum mechanics and thermodynamics of plasticity in relation to microscale deformation mechanisms, in *Constitutive Equations in Plasticity*, edited by A. S. Argon, MIT Press, Cambridge, Mass.

Rice, J. R. (1983), Constitutive relations for fault slip and earthquake instabilities, *Pure Appl. Geophys.*, *121*(3), 443–475.

Rice, J. R., N. Lapusta, and K. Ranjith (2001), Rate and state dependent friction and the stability of sliding between elastically deformable solids, *J. Mech. Phys. Solids*, *49*, 1865–1898.

Sayers, C., and M. Kachanov (1995), Microcrack-induced elastic wave anisotropy of brittle rocks, *J. Geophys. Res.*, *100*(B3), 4149–4156.

Scholz, C. H. (1968), Experimental study of the fracturing process in brittle rocks, *J. Geophys. Res.*, *73*(4), 1447–1454.

Scholz, C. H. (2002), *The Mechanics of Earthquake and Faulting,* 2nd ed., Cambridge Univ. Press, Cambridge, U. K.

Thomsen, L. (1986), Weak elastic anisotropy, *Geophysics*, *51*(10), 1954–1966.

Trefethen, L. N. (2000), *Spectral Methods in MATLAB*, vol. 10, SIAM, Philadelphia, Pa.

Wan, K.-T., S. Lathabai, and B. R. Lawn (1990), Crack velocity functions and thresholds in brittle solids, *J. Eur. Ceram. Soc.*, *6*, 259–268.

Wiederhorn, S. M., E. R. Fuller, and R. Thomson (1980), Micromechanisms of crack growth in ceramics and glasses in corrosive environments, *Met. Sci.*, *14*, 450–458.